



Automated Robot-Based Computed Tomography Trajectory Optimization using Differential Evolution in 3D Radon Space

Maximilian Linde^{1,3} · Wolfram Wiest¹ · Anna Trauth^{2,3} · Markus G. R. Sause³

Received: 31 March 2025 / Accepted: 19 May 2025
© The Author(s) 2025

Abstract

Limited accessibility of the X-ray hardware manipulating robots stemming from collision elements and the restricted workspace of the robots as well as areas of significant X-ray absorption are inherent characteristics of robot-based computed tomography scanning in subregions of large structures. The manual definition of trajectories is resource-intensive and results in substantial user influence on the resulting data quality. Therefore, this work proposes a method for the automated calculation of optimized (partial) circular scan trajectories for robot-based computed tomography. Specifically, a differential evolution algorithm is used to find global parametrization optima by estimating the reconstruction quality of trajectories. This estimation is based on a quantitative sampling quality metric in 3D Radon space, which is introduced in this work. The proposed method is evaluated on a test body from a region of limited accessibility within the strut mount of a car body. The reconstruction results are compared to those obtained from nearly 1000 reference trajectories. The results demonstrate that the proposed technique automatically generates trajectories that surpass the global optimum in data completeness of all reference trajectories. This methodology thus enables the elimination of user influence in trajectory parametrization.

Keywords Industrial computed tomography · Robot-based computed tomography · Trajectory optimization · CT data completeness · Limited accessibility

1 Introduction/Motivation

Trajectory optimization exhibits significant potential in industrial robot-based computed tomography (RCT) applications [1, 2]. In this context, the research community is

developing promising methodologies to achieve improved data quality [3] or reduced acquisition times with at least equivalent image quality [4] through the use of non-standard scanning trajectories. Trajectory optimizations can be categorized into approaches that focus on the imaging of a known geometry [5, 6], and those that aim to enhance the data completeness of a scan region [7, 8].

The computed tomography examination of partial regions in large full assembly, multimaterial components in a laboratory environment presents significant challenges for the application of RCT in automotive development. Typically, CT specialists are presented with dynamically changing inspection regions and tasks with daily frequency. The identification of an optimal trajectory for each specific inspection region is highly complex and challenging, with outcomes being significantly influenced by the user. Especially, accessibility-restricting elements of the object, as well as high X-ray absorption in the case of fully assembled large components, significantly limit trajectory selection. Trajectory optimization algorithms address this issue by autonomously generating optimal scan trajectories, thereby reducing the impact of user-dependent variability. Classical inquiries such

✉ Maximilian Linde
maximilian.linde1@porsche.de

Wolfram Wiest
wolfram.wiest1@porsche.de

Anna Trauth
trauth@wm.tu-darmstadt.de

Markus G. R. Sause
markus.sause@uni-a.de

¹ Dr. Ing. h.c. F. Porsche AG, Porscheplatz 1, 70435 Stuttgart, Germany

² Materials Mechanics Group, Technical University of Darmstadt, Franziska-Braun-Straße 3, 64287 Darmstadt, Germany

³ Institute of Materials Resource Management, University of Augsburg, Am Technologiezentrum 8, 86159 Augsburg, Germany

as the placement of seals, voids in cast components, meandering formations in adhesives, or traditional damage forensics imply trajectory optimization methodologies that aim to sample the region of interest (ROI) as comprehensively as possible. In such scenarios, it is often not feasible to define a specific geometry for which the trajectory should be optimized, as the geometry in question is not known in advance. Consequently, trajectory optimizations which aim to optimize the imaging of a desired geometry are typically not the appropriate tool in this context. Determining the optimal trajectory is highly complex, primarily due to limited accessibility caused by large test objects like entire car bodies and the presence of highly absorbent material combinations and potentially long X-ray paths through the large component.

Tuy's data sufficiency criterion serves as foundation for the analysis of data completeness in cone beam CT scans [9]. Based on this foundation, several approaches have been developed to assess the data completeness of arbitrary CT trajectories [10, 11]. The underlying idea is that to optimally reconstruct a point within a volume, the Radon transform of all possible planes through that point must be measured. The methodologies then quantify the degree to which this condition is met. To quantify the completeness of the entire volume, this analysis can be performed for each voxel within the volume. The methods have the limitation that the quantitative description is entirely independent of the scanned object and its material composition. Moreover, these methodologies are better characterized as quality assessment metrics for pre-existing trajectories, rather than optimization techniques, as they do not involve the selection or identification of optimal trajectories. Therefore Herl et al. [7] extend the approach by employing a greedy algorithm to identify the projection views that ensure optimal coverage of the Radon space, while simultaneously filtering out projection views that exhibit excessive X-ray absorption, thereby reducing the formation of metal artifacts. Schneider et al. [8] further developed this approach by applying an integer optimization method instead of a greedy algorithm.

The approaches in [7, 8] are based, like the majority of trajectory optimization methods in industrial RCT, on a starting set of predefined projection views on a sphere. The best possible projection views are selected from this set. In scanning scenarios of limited accessibility, we have already shown in previous work [2], that the reconstruction quality of trajectories is highly dependent on the chosen focus-detector distance (FDD). Additionally, the path planning problem remains, as the projection views can be arbitrarily distributed throughout the space. Even when the projection views are verified for accessibility, an additional, complex analysis is required for the path between the selected projection views. Therefore, despite numerous advancements, the application of (partial) circular trajectories remains the standard for industrial CT scans in laboratory settings today.

In this work, we consequently present a trajectory optimization method that identifies continuous circular trajectory intervals in scanning scenarios of limited accessibility within the laboratory environment of automotive development, aiming for maximum data completeness while minimizing strong metal artifacts after reconstruction. The presented methodology can define achievable trajectories of high information content for a variety of inspection tasks on large-scale components, such as entire automotive bodies.

Our objective function is based on a quantitative sampling completeness metric in 3D Radon space. In contrast to [10, 11], we do not examine the quantification of the measured Radon transformations through each point in the ROI. Instead, we pre-sample the Radon space of the ROI with features that correspond to planes in the spatial domain. These features encompass various orientations and positions of planes within the spatial domain. The quantification of data completeness for the trajectories is derived from the proportion of these features that are effectively sampled. We employ the differential evolution (DE) optimizer to improve the parametrization of respective (partial) circular trajectories. Assuming constant magnification, the focus-object-distance (FOD) and the trajectory tilt represent the parameters to be optimized. The trajectory tilt specifies how the respective circular trajectory is situated in space, with the initial trajectory lying in the xy -plane. Each trajectory tilt is specified by an extrinsic rotation in xy -sequence, with φ representing the rotation about the x -axis and θ the rotation about the y -axis in the coordinate system of the ROI, depicted in Fig. 1.

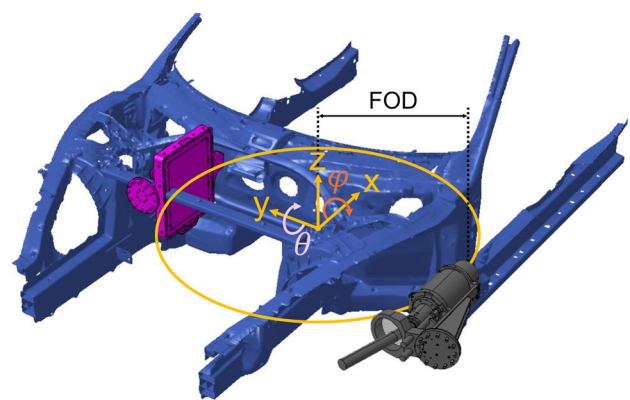


Fig. 1 Schematic illustration of the optimization parameters FOD, φ , and θ , exemplified by the target region investigated in this work in the area of the strut mount. The initial trajectory in the xy -plane is schematically depicted in orange. Rotations are performed in an extrinsic xy -order with respect to the depicted coordinate system. Note that in the illustrated projection geometry, the detector is highlighted in purple to indicate a potential collision scenario

2 Methodology

Optimizing a trajectory in relation to an objective function $\Phi(\zeta)$ is a highly complex, non-convex problem. To prevent getting trapped in local optima and instead find the global optimum, effective algorithmic approaches are required. The underlying general numerical optimization problem can be described by the search for the solution vector ζ^* at which the function $\Phi(\zeta)$ attains its minimum value:

$$\text{identify } \zeta^* | \Phi(\zeta^*) \leq \Phi(\zeta) \forall \zeta \tag{1}$$

with ζ and ζ^* denoting vectors of E real-valued parameters [12]. In the context of this study, we employ the DE optimizer, first introduced by Storm and Price [13] in 1995, to determine ζ^* . DE is categorized as an evolutionary algorithm due to its reliance on population-based techniques. In general, DE consists of an initialization step, followed by iterative mutation, recombination and selection procedures to improve a set of candidate solutions, steering towards an optimal outcome. In the following, we provide a brief explanation of each sub-process of the algorithm, closely following [13, 14], where further details can also be found.

First, N_p vectors, each consisting of E parameters, are randomly initialized within the upper and lower bounds for each parameter to produce the initial population $P_{\zeta,g0}$. The test loop then starts with the *differential mutation*, which generates new candidate solutions (mutation vectors $m_{i,g}$) by adding the scaled differences of randomly selected vectors r_1, r_2 of the current generation g to a third vector r_0 :

$$m_{i,g} = \zeta_{r0,g} + F \cdot (\zeta_{r1,g} - \zeta_{r2,g}), i = 0, 1, \dots, N_p - 1, g = 0, 1, \dots, g_{max}, F \in (0, 1+). \tag{2}$$

In this context, F is a constant factor regulating the differential variation ($\zeta_{r1,g} - \zeta_{r2,g}$). Subsequently, the mutation vectors are used in a crossover process, resulting in trial vectors $u_{i,g}$ that combine parameters from the current vector $\zeta_{i,g}$ and the mutation vector $m_{i,g}$:

$$u_{i,g} = u_{j,i,g} = \begin{cases} m_{j,i,g}, & \text{if } \text{rand}_j(0,1) \leq CR \text{ or } j = j_{rand} \\ \zeta_{j,i,g}, & \text{otherwise.} \end{cases} \tag{3}$$

Here, j ranges from 0 to $E - 1$ representing the parameter indices, and $CR \in [0, 1]$ denotes the crossover probability. The following selection process compares the objective function value of the trial vector against that of the current vector in the population:

$$\zeta_{i,g+1} = \begin{cases} u_{i,g}, & \text{if } \Phi(u_{i,g}) \leq \Phi(\zeta_{i,g}) \\ \zeta_{i,g}, & \text{otherwise.} \end{cases} \tag{4}$$

The population $P_{\zeta,g+1}$ is transferred back into the test loop. This process is repeated until convergence occurs or a prespecified stopping criterion is met.

Our implementation employs the DE method from the *scipy.optimize* module within the *SciPy* library [15]. We utilize the *rand/1/bin* strategy, which means that our base vector $\zeta_{r0,g}$ in Eq. 2 is selected randomly from the population. One scaled vector difference is added during the mutation process and binary crossover is applied, wherein each dimension is randomly chosen to be taken from either the trial vector $u_{i,g}$ or the existing vector $\zeta_{i,g}$. This strategy is exploration-oriented, meaning it promotes a diverse search across the solution space. Furthermore, the standard parameters of the DE algorithm from *scipy.optimize* are used, with a scaling factor of $F = 0.5$, and a crossover probability of $CR = 0.7$.

DE is designed to solve minimization problems. In the context of this work, we aim to maximize an objective function $\Phi(\zeta)$, which can be achieved by minimizing $-\Phi(\zeta)$. Consequently, Eq. 1 becomes:

$$\text{identify } \zeta^* | -\Phi(\zeta^*) \leq -\Phi(\zeta) \forall \zeta. \tag{5}$$

As outlined in Sect. 1, the objective function depends on the variable parameters of the trajectory: the trajectory radius, which corresponds to the FOD, and the trajectory tilt, which is defined by an extrinsic rotation in a xy-sequence in the coordinate system of the ROI. Here, φ denotes the rotation about the x-axis, while θ denotes the rotation about the y-axis. Accordingly, we use the nomenclature $T_{trajectory\ labeling}^{FOD,\varphi,\theta}$ for the trajectories. Furthermore, the function is influenced by constraint arguments that define spatial restrictions of the source and the detector (collision-free reachable space of the source K_s and the detector K_d , see [16] for further explanation), as well as the required minimum residual intensity percentage q_{thresh} . It is worth noting that the computation of K_s, K_d , as well as the residual intensity calculation requires the coarse, material-specific geometry of the object, which is generally available in industrial settings as CAD data. However, a representation of the usually unknown geometry in question within this object geometry is not necessary. The workflow for evaluating a parameter set FOD, φ, θ is depicted in Fig. 2 and will be further detailed in the following.

For each parameterization of $\Phi(\zeta)$, circular trajectories T_{mi} are defined, which contain N_v discrete projection views v_n with $n = 1, 2, \dots, N_v$, where v_n is defined as $\{location_{source}, location_{detector}, orientation_{source}, orientation_{detector}\}$. The object-detector distance (ODD) is currently set equal to the FOD, however it can be modified through a flexible ratio parameter. After the circular trajectories are defined, the objective function evaluates the residual intensity RI of the projection views using simulated X-ray projection images from aRTist [17] to avoid the formation of significant metal artifacts in the reconstructions, which are a common issue in full assembly components as plastic structures are combined

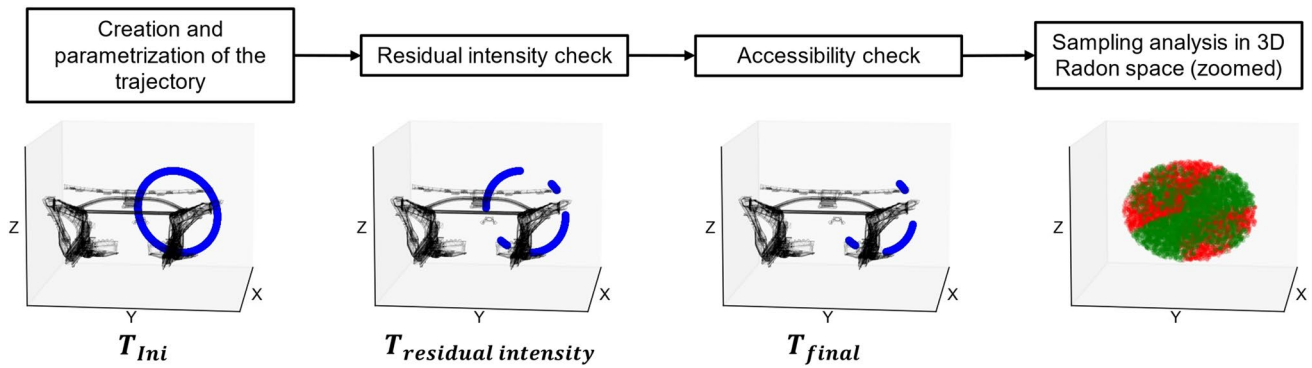


Fig. 2 Creation and evaluation workflow for a sample parameter set FOD, φ , θ of the region to be analyzed described in Section 3. X-ray source acquisition positions below each respective process step are depicted in blue, sampled features by the trajectory in the 3D Radon space are shown in green, and unsampled features in the 3D Radon space are represented in red

with high absorbing metal components [18]. For these steps, the method requires material-specific construction data of the component under investigation, which is typically available as prior knowledge. The goal is not to prevent smaller metal artifacts that may arise from components such as screws, but rather to avoid large blind spots in the reconstructed volume. Therefore, we define the argument q_{thresh} , which describes the percentage of the total number of pixels that may have a residual intensity below 10% of the maximum pixel value I_{max} to still be considered a valid projection view. We therefore adhere to the threshold value for the residual intensity recommended in ISO standard for non-destructive testing (DIN EN ISO 15708–2:2019) [19]. Since components are represented across multiple consecutive projection views in circular trajectories, we do not examine each projection view individually. Instead, we define an evaluation distance h for views to be evaluated. Consequently, we consider k intervals L_k that each consist of h projection views. The projection image of the central projection view of each interval $v_{central,k}$ is subjected to examination. If a projection view fails this examination, it is marked as unusable, and all projection views within the corresponding interval are discarded. After verifying the residual intensity, the trajectory contains the following entries:

$$T_{residual\ intensity} = \bigcup_{\{k|RI(v_{central,k}) < q_{thresh}\}} L_k, \tag{6}$$

where $RI(v_n)$ represents the relative proportion of pixels with an intensity $< 0.1I_{max}$. We recommend using evaluation distances of 10 degrees to ensure the detection of highly absorbing structures during rotation while keeping computational effort manageable. Subsequently, the objective function utilizes raycasting for the remaining source and detector positions of the projection views in $T_{residual\ intensity}$ to ascertain which lie within K_s and K_d respectively, defined by the condition:

$$T_{final} = \{v_n \in T_{residual\ intensity} | Inside(location_{n,source}, K_s) \wedge Inside(location_{n,detector}, K_d)\}. \tag{7}$$

Here, $Inside(point, area)$ is a function that determines whether $point$ is located within the region defined by $area$.

The current setup simulates the robotic CT system developed by the Fraunhofer EZRT [20]. Consequently, all v_n that are contained in T_{final} are characterized by being within the robot's workspace and exhibiting a collision-free inverse kinematics solution.

For the remaining valid projection views in T_{final} , the number of features sampled in the 3D Radon space is calculated, as schematically shown in Fig. 3.

We utilize the concept of the 3D Radon transform, which calculates the integral of a 3D object $f(\vec{x}) \triangleq f(x, y, z)$ over planes defined by their normal vector \vec{n} and the distance c to the imaging center o :

$$Rf(\vec{n}, c) = \int_{-\infty}^{+\infty} \int_{-\infty}^{+\infty} \int_{-\infty}^{+\infty} f(\vec{x}) \delta(\vec{x}^T \vec{n} - c) dx dy dz. \tag{8}$$

Herein, features in the 3D Radon domain represent planes in the spatial domain. The position vector of the features is defined by the normalized normal vector of the plane (indicating direction) and the distance from the plane to the imaging center (representing length), see Fig. 3. Each valid projection view represents a spherical cap in the 3D Radon space. Features that lie within an error tolerance d_f

$$d_f \approx \frac{|\xi| \cdot \pi}{D} \tag{9}$$

from the surface of the spherical cap are sampled by the corresponding projection view. Here, $|\xi|$ represents the distance of a feature in the Radon space to the origin, and D is the number of detector elements imaging the ROI along one detector dimension [21]. The planes of these features in the spatial domain intersect the trajectory and are therefore

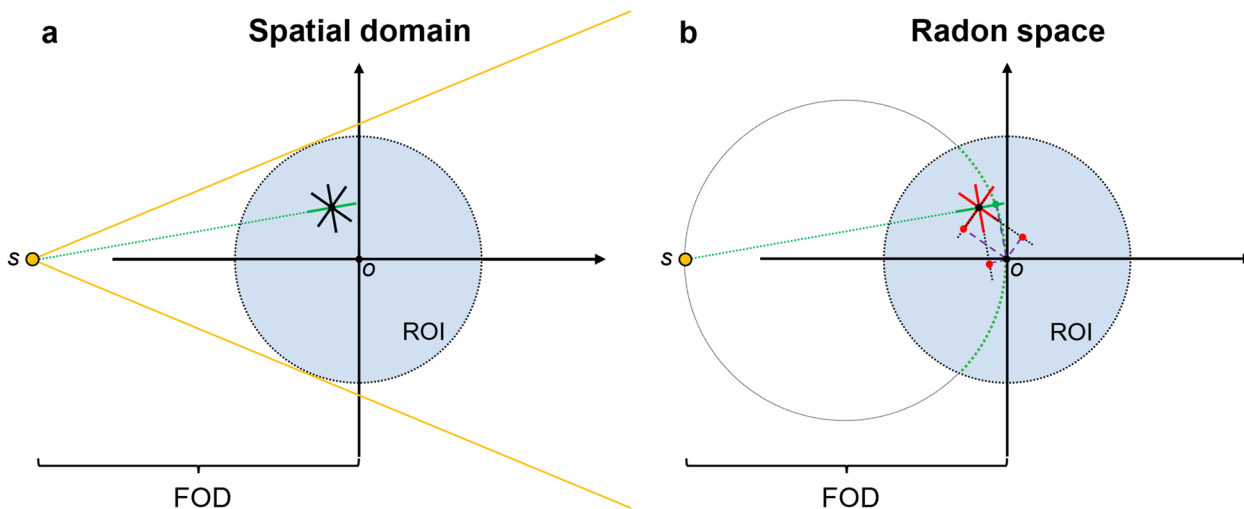


Fig. 3 Mapping of planes in the spatial domain to features in Radon space using the example of a single projection view with the X-ray source position s . Each plane is translated into a feature in Radon space. The position vector of features is defined by the normal vector of the corresponding plane and the distance of the plane to the imaging center o . **a)** 4 exemplary plane orientations at a position within the ROI. **b)** Depiction of the planes as features in Radon space. A projection view forms a circular cap (spherical cap in 3D) within the ROI, on which correctly sampled features (green) are located

correctly sampled according to Tuy’s cone beam reconstruction criterion [9]. Unlike the method by Amirkhanov et al. [22], we cannot mark all features within a torus generated for circular trajectories in the Radon space as sampled. This is because, in the case of partial circular trajectories, it cannot be guaranteed that the entire partial toroidal volume is sampled, as shown in Fig. 4.

In contrast to object- or geometry-specific trajectory optimization approaches, the exact geometry of the inspection region, specifically the geometry in question, is not known a priori. Therefore, the 3D Radon space is pre-sampled using

a random sampling that approximates a uniform distribution of features within the ROI to capture as many planar positions and orientations in the spatial domain as possible. Uniform feature placement is important, as a (partial) circular trajectory samples specific sectors of features in Radon space, see Fig. 4. Non-uniform distribution could lead to disproportionate sampling, where e.g., sampling one-third of the ROI may not correspond to one-third of the sampled features in Radon space, but rather to a significantly larger or smaller proportion. The number of features to be sampled was empirically established as 1000, which was found to

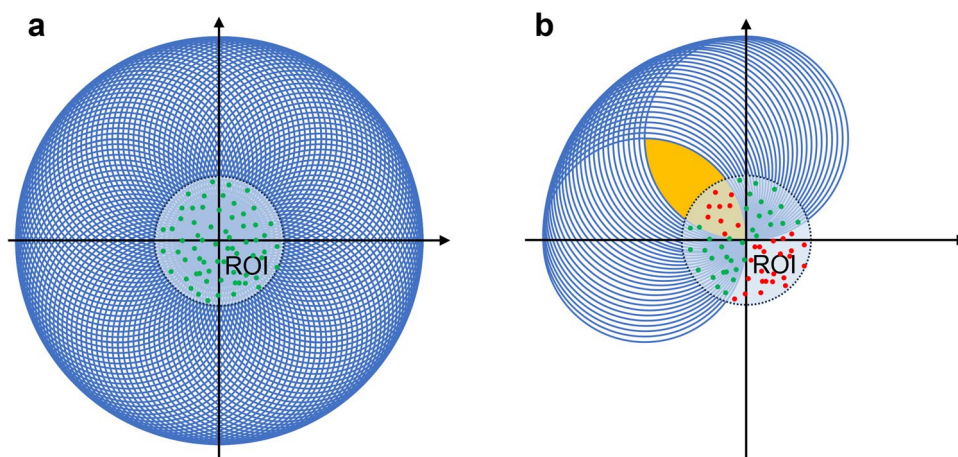


Fig. 4 Simplified representation of ROI cross-sections in the 3D Radon domain. Dots represent features that correspond to specific planes in the spatial domain. Red dots illustrate unsampled features while green dots depict sampled features. **a)** Circular trajectory with full sampling. The surfaces of the spherical caps (circular caps in 2D) cover the entire torus. **b)** 90° partial circular trajectory, where the orange-shaded region lies within the (partial) torus but is not covered by the surfaces of the spherical caps (circular caps in 2D)

be sufficient. The objective function ultimately provides the number of sampled features as a scalar value:

$$\Phi(FOD, \varphi, \theta; K_s, K_d, RI) = \text{number of sampled features.} \quad (10)$$

FOD , φ , and θ represent the optimization parameters. K_s , K_d , and RI represent the constraint arguments, with K_s and K_d being system-defined parameters and RI being a user-defined parameter. The relative value of the sampled features in Radon space by the spherical caps inherent in the selected trajectory additionally serves as a figure of merit to quantify the extent of data completeness within the ROI:

$$FOM_{\text{completeness}} = \frac{\text{features}_{\text{sampled}}}{\text{features}_{\text{total}}} \cdot 100. \quad (11)$$

Once the DE algorithm converges or the stopping criterion is met, the features sampled by the resulting (partial) circular trajectory in the Radon domain are calculated. As a stopping criterion, the number of iterations or a time limit can be established. Features sampled by the trajectory are then removed from the 3D Radon space. If the 3D Radon domain still contains unsampled features and fewer than the maximum number of user-defined partial circular trajectories (i.e. runs of the DE algorithm) have been generated, the DE is restarted with the updated set of features that remained unsampled up to that point. To further elucidate the procedure, Table 1 presents pseudocode that describes the methodology as an algorithmic workflow.

3 Results

For the validation of the proposed methodology, an inspection region on a vehicle body, depicted in Fig. 5, is used with the aim of simulating scans on vehicle bodies and the associated limitations in accessibility and attenuation as closely as possible to real-world conditions. The center of the ROI is positioned at the center of the socket for the strut mount on the driver's side. For other inspection regions, the user can generally select the center of the ROI at arbitrary coordinates on the object under inspection. It is important to note that the axis of the circular trajectory is required to pass through this center point of the ROI. The ROI consists of a simulated aluminum cast component that contains a centrally positioned real air pore that was modeled from a CT scan of a cast component. Additionally, four artificial air spheres are integrated in-plane to demonstrate sampling effects. It is important to note that pores in cast components represent only a subset of the examination subjects for RCT scans on entire vehicle bodies. However, this examination subject is especially suitable for validating the technique as an extreme case, as pores and spheres obtain multidirectional surface

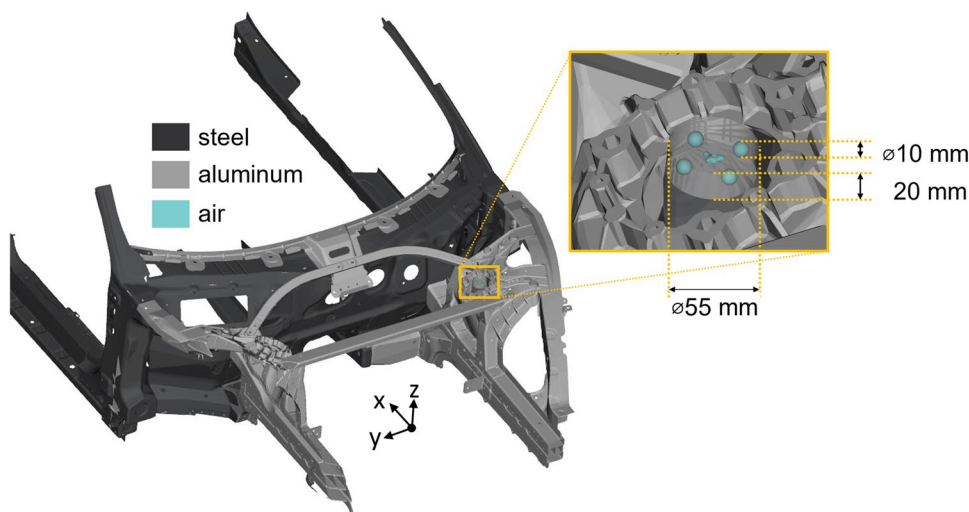
Table 1 Pseudocode of the algorithmic workflow for improving the parametrization of circular trajectories presented in this study

Pseudocode of the algorithmic workflow	
1.	Initialize the Radon space with uniformly distributed features.
2.	Initialize the population with randomly created parametrizations $\zeta = (FOD, \varphi, \theta)$.
3.	Evaluate each parametrization by computing the number of sampled features using equation 10.
4.	While the termination condition is not satisfied do: <ol style="list-style-type: none"> Create mutation vectors using the mutation strategy in equation 2. Create trial vectors using crossover in equation 3. Evaluate the number of sampled features using equation 10: <ol style="list-style-type: none"> Generate circular trajectories T_{mi} from trial vectors, apply filtering step of equation 6 to obtain $T_{\text{residual intensity}}$ followed by the filtering step of equation 7 to obtain T_{final}. Calculate the number of sampled features of T_{final} in Radon space. Select the better of each pair (trial vs. parent) for the next generation using equation 4.
5.	End While

vectors and can therefore only be fully reconstructed if the Radon space has been properly sampled by the trajectory. The aim of the simulation experiment is to optimally sample the ROI and achieve ideal reconstruction results for the air components.

We conduct a comparison of the proposed methodology with industrial standard circular CT trajectories at a magnification of 2 across various tilt angles. Three distinct FDDs with lengths of 800 mm, 1050 mm and 1300 mm are employed to generate the trajectories. The tilt angles are varied within a range of 0° to 170° , with increments of 10° . These variations encompass both the tilt angles around the x-axis (φ) and the y-axis (θ). Consequently, these configurations yield a total of 972 comparative trajectories. Larger FDDs are excluded from consideration due to excessively long exposure times. Each initial trajectory consists of 3000 equiangularly distributed projections on a circular geometry. The restriction parameters K_s , K_d and RI from Eq. 10 are applied to all trajectories, filtering the initial projections to produce the final trajectories for comparison, with q_{thresh} in Eq. 6 being empirically set to 20% for this scenario.

Fig. 5 Inspection region in the strut tower on the driver's side of a vehicle body. An aluminum test component is installed in the area of the strut mount

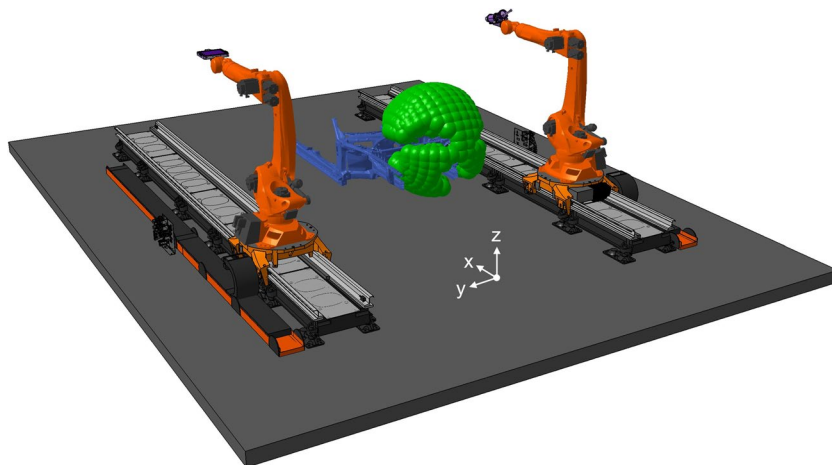


For the simulations, the X-ray parameters are configured as follows: The acceleration voltage is specified as 225 kV, while the tube current is set to 0.89 mA. This exhausts the maximum power limit of the simulated source. The exposure time is dynamically regulated by the X-ray simulation software, aRTist, to ensure that the background intensity remains at 90% of the maximum gray value for each gain image. Additionally, a flat-field correction is automatically applied to each projection image. A 2500×2500 pixel² flat panel detector with a pixel distance of 100 μm is utilized in this study. A 1 mm aluminum filter is applied into the setup. The ROI is reconstructed into CT volumes utilizing a voxel grid of size 2500^3 , where each voxel has a dimension of 100 μm . All reconstructions are executed using the algebraic reconstruction technique (ART), which is integrated within the CERA 6 CT imaging software (Siemens Healthineers AG). The test specimen is positioned in the system so that the test region is centrally aligned between the linear axes to make optimal use of the robot's working space. Additionally, the body is elevated by approximately 1 m to enable the

integration of vertical projection directions. For the calculation of the collision-free reachable spaces, K_s and K_d , setup geometries (support structures/lifting straps) are disregarded for reasons of simplification. The positioning of the car body and the collision-free reachable space of the detector, K_d , are illustrated in Fig. 6.

Figure 7 illustrates the relative values of the $FOM_{\text{completeness}}$ for the comparison trajectories using color coded representation. Notably, across all three analyzed FODs, similar trajectory tilts consistently result in comparable outcomes. This behavior can be attributed to the filtering of projection views, which is driven by either insufficient residual intensity in resulting projections or limited accessibility, affecting similar regions. In this particular inspection region, there is a tendency for accessibility to improve slightly with increasing FODs. Consequently, higher FODs exhibit higher sampling scores in the Radon space. However, this behavior is not universally applicable. Depending on the inspection region, lower FODs can also lead to higher accessibility and, therefore, better sampling outcomes.

Fig. 6 Positioning of the test specimen within the kinematic digital twin of the system in DELMIA V5. The area shown in green represents the collision-free reachable space K_d of the detector, which can be calculated using a developed add-on tool, described in [16]. Note that there also exists a collision-free reachable space K_s of the source, which is not plotted here for visualization purposes



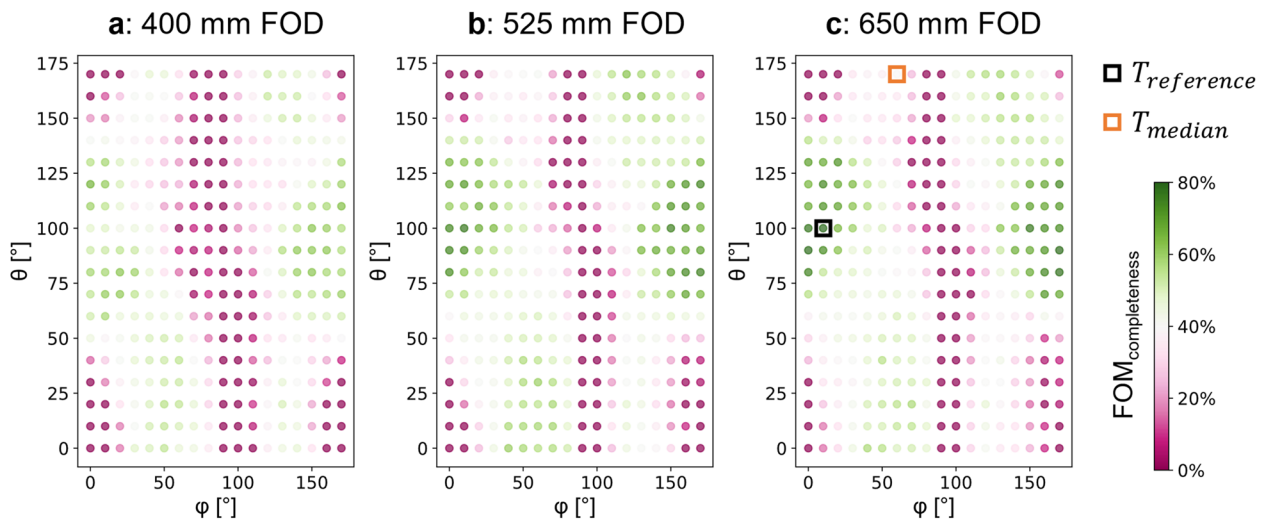


Fig. 7 Color coded representation of the $FOM_{completeness}$ of the comparison trajectories. Phi (ϕ) describes the rotation of the circular orbit around the x-axis, theta (θ) describes the rotation of the circular orbit around the y-axis. Plot **a**) references a FOD of 400 mm, plot **b**) a FOD of 525 mm and plot **c**) a FOD of 650 mm. The trajectory of the configuration $T^{650,10,100}$ exhibits the highest sampling efficiency at 79.3% and is denoted as $T_{reference}$, the trajectory of the configuration $T^{650,60,170}$ represents the median efficiency at 40.1% and is denoted as T_{median}

Additionally, the significant influence of trajectory tilts on sampling quality becomes evident. While the best comparison trajectory, $T_{reference}$, samples 79.3% of the features in the Radon space, the median trajectory, denoted as T_{median} , samples only 40.1% of the features in the Radon space. This observation further emphasizes the substantial user influence in trajectory selection and highlights the necessity of minimizing this influence as much as possible.

In the following analysis, the best comparison trajectory $T_{reference}$ as well as the median trajectory T_{median} from the comparison trajectory sets are selected to compare their qualitative and quantitative performance with the trajectories generated by the optimization technique proposed in this work. Furthermore, a supplementary comparison trajectory, $T_{reference\ large}$, is constructed. It incorporates the projection directions of the best-performing comparison trajectory, $T_{reference}$, while matching the number of projections used in the final trajectory generated by the proposed algorithm. Table 2 summarizes the notations of the relevant trajectories.

We simulate three iterations of the described DE algorithm. We limit ourselves to three iterations, as the added value of additional samplings per iteration significantly decreases due to already sampled regions. Furthermore, this constraint helps to keep the total number of projections within the commonly used and feasible ranges within the lower to mid four-digit projection counts. Features sampled by the trajectory in a previous iteration are excluded from consideration in the subsequent iteration. This ensures that only unsampled features are targeted in the subsequent iterations.

As can be observed in the first row of Table 3, the resulting trajectory from the first iteration of the DE algorithm, $T_{optimized1}$ samples 84.5% of the features in Radon space, which is 5.2% more than the best trajectory from the comparison sets, $T_{reference}$. It is notable that the orientation of $T_{optimized1}$ closely resembles the orientation of $T_{reference}$ and that $T_{reference}$ does not yet represent the global maximum of the objective function. After the second iteration of the DE algorithm, the trajectory $T_{optimized2}$ is obtained. This trajectory samples an additional 8.8% of the features in the Radon space and thus achieves a $FOM_{completeness}$ value of 93.3%. Following the third iteration of the DE algorithm, the trajectory $T_{optimized3}$ is obtained. It samples an additional 2.6% of the features in Radon space, resulting in a total coverage of 95.9% of the features for $T_{optimized3}$. The spatial arrangement of the projection views for each trajectory is depicted

Table 2 Notations of the trajectories used in the manuscript as well as their corresponding full nomenclature and number of incorporated projections

Notation	Complete nomenclature ($T_{trajectory\ labeling}^{FOD,\phi,\theta}$)	Number of projections
T_{median}	$T_{median}^{650,60,170}$	835
$T_{reference}$	$T_{reference}^{650,10,100}$	1426
$T_{reference\ large}$	$T_{reference\ large}^{650,10,100}$	3787
$T_{optimized1}$	$T_{iteration1}^{547.5,5,89.6}$	1428
$T_{optimized2}$	$T_{optimized2} = T_{iteration1}^{547.5,5,89.6} \cup T_{iteration2}^{548.1,152.1,109.2}$	2619
$T_{optimized3}$	$T_{optimized3} = T_{iteration1}^{547.5,5,89.6} \cup T_{iteration2}^{548.1,152.1,109.2} \cup T_{iteration3}^{615.5,36.2,125.1}$	3787

Table 3 Quantitative analysis of the volumes reconstructed from the trajectories

	Better when	T_{median}	$T_{reference}$	$T_{reference\ large}$	$T_{optimized1}$	$T_{optimized2}$	$T_{optimized3}$
FOM _{completeness} [%]	↑ (higher)	40.1	79.3	79.6	84.5	93.3	95.9
surface deviation less than 100 μm [%]	↑ (higher)	28.1	83.9	83.1	93.7	96.7	96.8
Chamfer distance [mm]	↓ (lower)	0.4759	0.2910	0.2930	0.2463	0.2389	0.2403
Volume difference [mm ³]	↓ (lower)	198.3	40.4	40.5	18.7	10.5	8.7

in Fig. 8. Note that since our objective is to optimize data completeness in the ROI rather than minimizing acquisition time, all projection views of successive iterations of the DE algorithm are incorporated into the resulting trajectories. This approach ensures the integration of the maximum amount of available information, analogous to conventional industrial CT, where circular acquisition trajectories of 360° are employed despite the theoretical sufficiency of a trajectory angle of 180° plus the cone beam opening angle.

For qualitative analysis, Fig. 9 provides mid plane cross-sectional images of the CT volumes resulting from the trajectories, as well as a three-dimensional rendering of the nominal-actual comparison of the air components with the ground truth STL model. For the nominal-actual

comparisons of the 3D volumes, the advanced surface determination tool in *VGSTUDIO MAX 2023.4 (Volume Graphics GmbH)* is used. The ground truth STL model of the air structures is employed as the initial contour, with the search distance set to 1 mm. The maximum allowable deviation in both positive and negative direction is set to 0.1 mm. It should also be noted that the exemplary cross-sectional images are only of limited significance, as they depict the actual state in just two planes. A slightly different rotation in the cross-sectional images could result in an entirely different visual impression.

It is noticeable that the trajectories $T_{reference}$, $T_{reference\ large}$, and $T_{optimized1}$ exhibit very similar artifact directions and characteristics. This can be attributed to the use of very similar

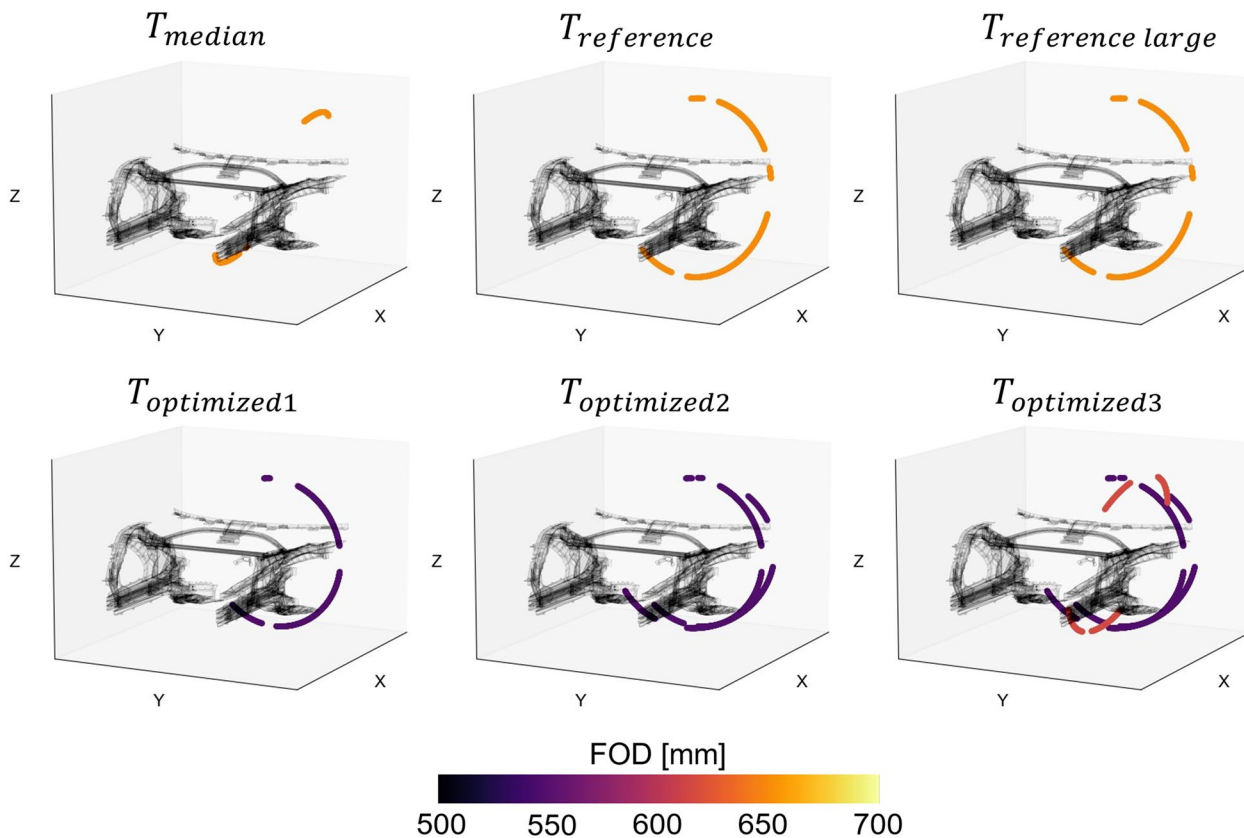


Fig. 8 Positions of the X-ray source derived from the projection views along each individual trajectory

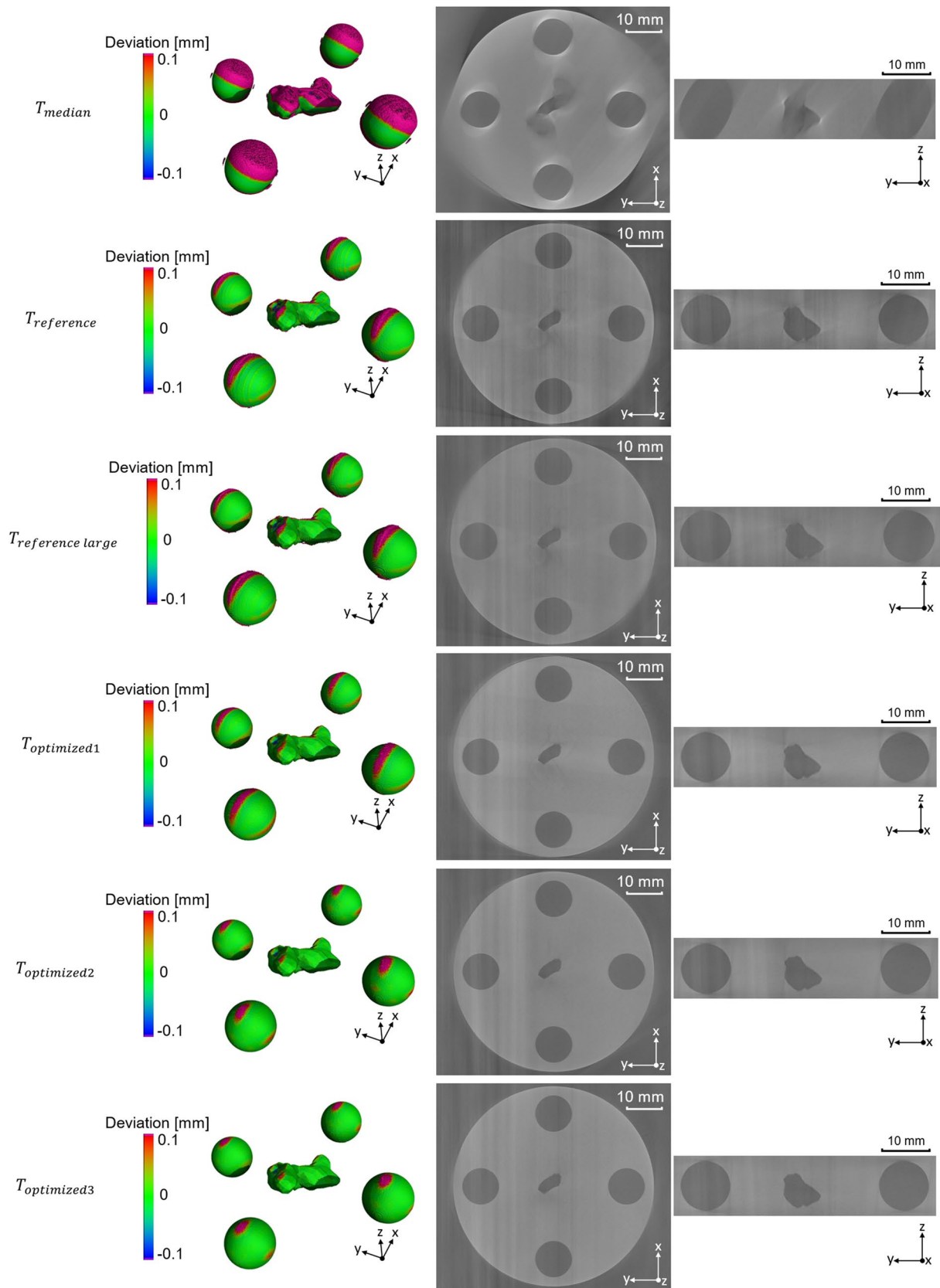


Fig. 9 Qualitative comparison of the reconstructed volumes resulting from the trajectories

acquisition angles, respectively the same angular ranges of $T_{reference}$ and $T_{reference\ large}$. Especially the artifacts located along a line extending approximately from 4 o'clock to 10 o'clock in the top view of $T_{optimized1}$ appear slightly less pronounced compared to $T_{reference}$, which correlates with the 5.2% higher rating of the $FOM_{completeness}$ metric. The qualitative impression of T_{median} is, as expected, significantly worse, confirming the low sampling quality. Only the edges within the equatorial region of the air volumes could be sampled, as the trajectory was only able to sample these tangentially with X-rays. In contrast, the polar regions lacked sufficient horizontal projections, see Fig. 8, preventing the acquisition of usable information. $T_{optimized2}$ demonstrates another reduction in artifacts compared to $T_{optimized1}$, $T_{reference}$, and $T_{reference\ large}$ particularly visible in the 3D visualization of the polar regions of the air components. However, the lemon-like shape of the air spheres observed in the side view, caused by missing wedge artifacts, persists because the artifacts in the central polar regions remain present, and the cross-sectional image passes precisely through the center of these regions. $T_{optimized3}$ delivers the best results in the visual analysis. However, the improvement over $T_{optimized2}$ is not enormous and correlates with the additional sampling of only 2.6% in the $FOM_{completeness}$. The 3D view reveals that artifacts persist in the polar regions of the air structures. This is due to the test object preventing projections within the xy-plane. Such projection views are either difficult to access or, when accessible, exhibit insufficient residual intensity. Achieving these projections would require penetrating several decimeters of aluminum, which is not feasible with the simulated source. This phenomenon is also observed in the comparative trajectories shown in Fig. 7, where trajectories within the xy-plane exhibit a very low $FOM_{completeness}$ value. It can therefore be concluded that, under the given conditions, a complete sampling of the Radon space is fundamentally unattainable for this ROI, as the required projection views in the xy-plane cannot be acquired.

The quantitative analysis of the reconstructed volumes presented in Table 3 further supports the qualitative results.

The results of the $FOM_{completeness}$ metric highlight the superior performance of the proposed technique. The $FOM_{completeness}$, as described above, serves as the basis of the selection algorithm. The resulting trajectory from three iterations of the presented algorithm achieves a $FOM_{completeness}$ value of 95.9%, whereas the best of the comparison trajectories reaches only 79.3% in $T_{reference}$, respectively 79.6% in $T_{reference\ large}$. While the proposed technique enables an almost complete data acquisition with minimal user intervention, even the best comparison trajectory cannot match its performance, also not when using the same number of projections. This is primarily due to the lack of directional information in $T_{reference}$ and $T_{reference\ large}$.

The surface deviation of less than 100 μm to the CAD ground truth further corroborates the observed trend and closely aligns with the values of the $FOM_{completeness}$. While the median trajectory, T_{median} , achieves less than 30% surface correspondence, the best of the comparison trajectories, $T_{reference}$, demonstrates 83.9% surface agreement, with $T_{reference\ large}$ nearly matching its value. This again underscores the substantial impact of trajectory selection on data quality in scans of large-scale components. With the trajectories generated by the proposed technique, surface correspondence compared to $T_{reference}$ in our scenario can be improved by an additional 9.8%, 12.8% and 12.9%, respectively. The chamfer distance (CD) [23, 24] quantifies the average distance between the nearest points a and b of two point sets A and B , enabling the assessment of similarity between the ground truth STL file of the air components and the STL files of the air components generated from the reconstructed volumes:

$$CD(A, B) = \frac{1}{|B|} \sum_{b \in B} \min_{a \in A} \|b - a\| + \frac{1}{|A|} \sum_{a \in A} \min_{b \in B} \|a - b\|. \quad (12)$$

The respective STL files were created using object conversion in *VGSTUDIO MAX 2023.4 (Volume Graphics GmbH)* in "accurate" mode (point reduction tolerance: 0.025 mm) without simplification. This metric also reveals a significant drop in performance for the trajectory T_{median} . $T_{optimized1}$ once again outperforms the best of the comparison trajectories. Additionally, $T_{optimized2}$ continues the observed trend of steady improvement. The slightly elevated CD of $T_{optimized3}$ may result from an uneven distribution of deviations. For instance, a small number of points with larger deviations can increase the CD, even if most of the surface is closer to the ground truth.

A more complete sampling reduces the volume difference by mitigating the prominent missing wedge artifacts. This further reaffirms the superior performance of the presented technique with each iteration.

In summary, all metrics exhibit the same trend. The DE algorithm selects higher-quality trajectories based on the $FOM_{completeness}$, reduces user influence, and can achieve further improvements through subsequent iterations by incorporating additional sampling angles.

In the context of this work, we deliberately refrain from applying grayscale-based reference metrics such as the Structural Similarity Index, as the creation of a ground truth is not feasible due to limited accessibility and excessive X-ray attenuation. Additionally, we anticipate a significant user influence in the selection of the slice plane on which the evaluations will be conducted.

4 Conclusion

This work introduces a broadly applicable trajectory optimization technique for RCT scans of large components characterized by limited accessibility. The technique is designed to maximize the data completeness of the desired ROI while mitigating the formation of metal artifacts. The DE optimizer is employed to identify optimal (partial) circular trajectories, with the objective function optimizing data completeness in Radon space while considering metal artifact formation and accessibility of the X-ray hardware manipulating robots. The trajectory radius and trajectory tilt angles serve as flexible optimization parameters. We demonstrated that the proposed technique for verifying data completeness in Radon space correlates well with other evaluation metrics. The designed (partial) circular trajectories achieve significantly higher percentages of sampled features in Radon space than conventional trajectories simulated for comparison, thereby demonstrating enhanced data completeness. The presented technique enables the delivery of optimal data in limited accessibility scan regions while eliminating significant user influence in trajectory selection. With the press of a button, results can be achieved that surpass the global optimum of nearly 1000 analyzed comparison trajectories.

Because the technique does not require any prior knowledge about the specific issue and only necessitates the selection of the desired scan region in the material-defined CAD model, it can be utilized for a wide range of inquiries in defect forensics.

Due to limited resources, the study is based on simulated data. However it has already been demonstrated that such trajectory optimization methods can also be executed on the actual system [1] though several challenges still need to be addressed for successful application on the actual system. For example, while the calculation of collision-free reachable spaces for the source K_s and detector K_d provides a good approximation, projection views in boundary areas should be manually verified prior to scanning. Similarly, the unmodeled curvature of the high-voltage cable of the X-ray source presents another factor that needs to be considered. Additionally, the real robots exhibit absolute positioning errors that are not accounted for in the simulation. Consequently, calibration methods like e.g. [25, 26], that compensate for these absolute positioning errors are essential for applying the methodology in real-world conditions.

Author Contributions M.L.: conceptualization, methodology, data curation, software, validation, visualization, writing – original draft; W.W.: supervision, writing – review and editing; A.T.: supervision, writing – review and editing; M.S.: supervision, writing – review and editing. All authors reviewed the manuscript.

Funding This work was funded by the Dr. Ing. h.c. F. Porsche AG and facilitated through collaborative research between academia and industry in partnership with the University of Augsburg. The method presented is not currently available for commercial use, and there is no assurance of its future availability.

Data Availability Not applicable.

Code Availability Not applicable.

Declarations

Conflict of interest The authors declare no competing interests.

Open Access This article is licensed under a Creative Commons Attribution-NonCommercial-NoDerivatives 4.0 International License, which permits any non-commercial use, sharing, distribution and reproduction in any medium or format, as long as you give appropriate credit to the original author(s) and the source, provide a link to the Creative Commons licence, and indicate if you modified the licensed material. You do not have permission under this licence to share adapted material derived from this article or parts of it. The images or other third party material in this article are included in the article's Creative Commons licence, unless indicated otherwise in a credit line to the material. If material is not included in the article's Creative Commons licence and your intended use is not permitted by statutory regulation or exceeds the permitted use, you will need to obtain permission directly from the copyright holder. To view a copy of this licence, visit <http://creativecommons.org/licenses/by-nc-nd/4.0/>.

References

1. Bauer, F., Forndran, D., Schromm, T., et al.: Practical part-specific trajectory optimization for robot-guided inspection via computed tomography. *J. Nondestruct. Eval.* **41**, 55 (2022)
2. Linde, M., Wiest, W., Trauth, A., et al.: Selecting Feasible Trajectories for Robot-Based X-ray Tomography by Varying Focus-Detector-Distance in Space Restricted Environments. *J. Nondestruct. Eval.* **43**, 65 (2024)
3. Schneider L-S, Thies M, Schielein R et al.: Learning-based Trajectory Optimization for a Twin Robotic CT System. In: Proc. 12th Conference on Industrial Computed Tomography (iCT). **27**, 1–8 (2022)
4. Fischer, A., Lasser, T., Schrapp, M., et al.: Object specific trajectory optimization for industrial x-ray computed tomography. *Sci. Rep.* **6**, 19135 (2016)
5. Matz A, Holub W, Schielein R.: Trajectory optimization in computed tomography based on object geometry. In: 11th Conference on Industrial Computed Tomography, Wels, Austria (iCT 2022). (2022)
6. Brierley, N., Bellon, C., Lazaro Toralles, B.: Optimized multi-shot imaging inspection design. *Proc. Royal Soc. A: Math., Phys. Eng. Sci.* **474**, 20170319 (2018)
7. Herl, G., Hiller, J., Maier, A.: Scanning trajectory optimisation using a quantitative Tuybased local quality estimation for robot-based X-ray computed tomography. *Nondestruct. Test. Eval.* **35**, 287–303 (2020)
8. Schneider L-S, Herl G, Maier A.: Integer Optimization of CT Trajectories using a Discrete Data Completeness Formulation. arXiv preprint arXiv:2402.10223. (2024)
9. Tuy, H.K.: An inversion formula for cone-beam reconstruction. *SIAM J. Appl. Math.* **43**, 546–552 (1983)

10. Maier A, Kugler P, Lauritsch G et al.: Discrete estimation of data completeness for 3D scan trajectories with detector offset. In: Bildverarbeitung für die Medizin 2015: Algorithmen-Systeme-Anwendungen. Proceedings des Workshops vom 15. bis 17. März 2015 in Lübeck. 47–52 (2015)
11. Liu, B., Bennett, J., Wang, G., et al.: Completeness map evaluation demonstrated with candidate next-generation cardiac CT architectures. *Med. Phys.* **39**, 2405–2416 (2012)
12. Price, K.V.: Differential Evolution. In: Zelinka, I., Snášel, V., Abraham, A. (eds.) *Handbook of Optimization: From Classical to Modern Approach*, pp. 187–214. Springer, Berlin Heidelberg, Berlin, Heidelberg (2013)
13. Storn R, Price K.: Differential evolution—a simple and efficient adaptive scheme for global optimization over continuous spaces. *International computer science institute*. (1995)
14. Price, K., Storn, R., Lampinen, J.: The Differential Evolution Algorithm. In: *Differential Evolution: A Practical Approach to Global Optimization*, pp. 37–134. Springer, Berlin Heidelberg, Berlin, Heidelberg (2005)
15. Virtanen, P., Gommers, R., Oliphant, T.E., et al.: SciPy 1.0: fundamental algorithms for scientific computing in Python. *Nat. Methods* **17**, 261–272 (2020)
16. Linde M, Wiest W, Trauth A et al.: Trajectory optimization for few-view robot-based CT: Transitioning from static to object-specific acquisition geometries. *Tomography of Materials and Structures*. 100058 (2025)
17. Bellon C, Deresch A, Gollwitzer C et al.: Radiographic simulator aRTist: version 2. In: 18th World Conference on nondestructive testing. 16–20 (2012)
18. Amirkhanov, A., Heinzl, C., Reiter, M., et al.: Projection-based metal-artifact reduction for industrial 3D X-ray computed tomography. *IEEE Trans. Visual Comput. Graphics* **17**, 2193–2202 (2011)
19. Deutsches Institut für Normung (DIN), Europäische Normungsorganisation (EN), Internationale Organisation für Normung
Zerstörungsfreie Prüfung – Non-destructive testing - Radiation methods for computed tomography - Part 2: Principles, equipment and samples (ISO 15708–2:2017); German version EN ISO 15708–2:2019
20. Holub, W., Brunner, F., Schön, T.: Roboct-application for in-situ inspection of joint technologies of large scale objects. *Int. Symp. Digit. Industr. Radiol. Computed Tomography* **11**, 1–7 (2019)
21. Buzug TM.: Computed tomography: from photon statistics to modern cone-beam CT. *Soc Nuclear Med.* **50**, (2009)
22. Amirkhanov, A., Heinzl, C., Reiter, M., et al.: Visual optimality and stability analysis of 3DCT scan positions. *IEEE Trans. Visual Comput. Graphics* **16**, 1477–1486 (2010)
23. Barrow HG, Tenenbaum JM, Bolles RC et al.: Parametric correspondence and chamfer matching: Two new techniques for image matching. In: *Proceedings: Image Understanding Workshop*. 21–27 (1977)
24. Akmal Butt, M., Maragos, P.: Optimum design of chamfer distance transforms. *IEEE Trans. Image Process.* **7**, 1477–1484 (1998). <https://doi.org/10.1109/83.718487>
25. Weiss A, Wittl S, Herl G et al.: Simulated and experimental evaluation of the accuracy of twin robotic CT systems. In: 12th conference on industrial computed tomography (iCT). (2023)
26. Rückert D, Butzhammer L, Wittl S et al.: Uncalibrated CT Reconstruction for One-Shot Scanning of Arbitrary Trajectories. In: 13th conference on industrial computed tomography (iCT). (2024)

Publisher's Note Springer Nature remains neutral with regard to jurisdictional claims in published maps and institutional affiliations.